



Cassini Bistatic Radar Experiments: Preliminary Results on Titan's Polar Regions

Giancorrado Brighi¹

Received: 20 July 2022 / Revised: 18 August 2022 / Accepted: 26 August 2022 / Published online: 10 September 2022
© The Author(s) 2022

Abstract

In bistatic radar observations, reflected echoes from the surface of a target planet can be analyzed to infer its surface statistics and near-surface constituents. In this work, a preliminary inspection of two X-band bistatic radar observations gathered by the Cassini spacecraft about Titan's polar regions is presented. Profiles of relative dielectric constant and root-mean-square (rms) surface slope are provided as outputs of the analysis, discussed, and compared with the present knowledge of Titan geomorphology. For the assessment of the rms slope, proportional to the spectral broadening of reflected echoes, a basic fitting procedure was applied to the received spectra using a Gaussian template, to later evaluate the full-width half-maximum of the fitting curve. The dielectric constant was computed from the power ratio between orthogonally circularly polarized components of signal reflections from Titan. Dielectric constant estimates are, on average, consistent with the expected materials covering the dry surfaces of the planet, while slightly low values were found over the seas. The rms slopes are generally low compared to past bistatic observations of other targets. Titan's north polar seas are revealed to feature an unprecedented smoothness, with 0.01° of slope as an upper bound. Similar values were inferred for isolated spots in the southern pole, hinting at the possible presence of basins filled with liquid hydrocarbons. The main issues with the analysis are emphasized throughout the document, and some ideas for future work are presented in the conclusions.

Keywords Cassini · Bistatic radar · Titan · Rms surface slope · Dielectric constant

1 Introduction

Bistatic radar (BSR) experiments have been employed for years to remotely probe planetary surfaces, complementing Earth-based and orbiter-based monostatic observations. When a radio signal is sent to a target planet and reflected from its surface, terrain's features with scales proportional to radar wavelengths interact with it. A proper processing of the scattered echoes can provide information about root-mean-square (rms) slope (ζ), near-surface relative dielectric constant (ϵ) and density (ρ) of the target [1]. Measurements have been inferred about the Moon, Mars [2], Venus [3], smaller bodies like asteroid Vesta [4] and comet 67P/CG, by means of this radio science probing technique.

The advantage of a bistatic geometry, compared to a monostatic radar, is that the spatial separation between transmitter and receiver can be exploited to characterize target's scattering properties in a more complete way than looking at pure backscattering, with the additional help of the reception performance of a modern ground-based facility [1]. On the other hand, Earth-based observations are usually restricted to equatorial bands of target planets, while the vicinity of a flying probe to the target planet makes it possible to observe space objects at a variety of latitudes and longitudes [2].

Originally implemented as downlink “experiments of opportunities”, the first satisfying results of bistatic radar experiments probing planetary surfaces led to a more planned out employment of this technology in various missions [1]. During its science phase, the Cassini orbiter pointed its High-Gain Antenna (HGA) to the surface of the largest moon of Saturn, Titan, and used its Radio Science Subsystem to perform 13 downlink near-forward quasi-specular bistatic observations of the planet, in three available frequency bands: S-band, X-band and Ka-band (Fig. 2). Deep Space Network (DSN) stations were employed as

✉ Giancorrado Brighi
giancorrado.brighi@unibo.it

¹ Department of Industrial Engineering, Alma Mater Studiorum-University of Bologna, Via Fontanelle 40, Forlì 47121, FC, Italy

Earth-based receivers to collect echoes from the target planet. These remote observations were scheduled to illuminate a variety of Titan's morphological terrains, from equatorial seas of organic sand, to the oceans of liquid hydrocarbons occupying the majority of the planet's North Pole.

In this work, a preliminary analysis of a subset of the available Cassini bistatic radar data is performed. The evolution of rms surface slope and dielectric constant along different specular point ground tracks is computed, discussed and compared with results gathered by ground-based [5] and Cassini RADAR [6] observations of Titan. The absence of any published analysis of Cassini bistatic radar data makes the outputs of this research unique.

In Sect. 2, the problem of surface scattering is briefly introduced, with a focus on those aspects that are useful to explain the bistatic radar experiment (Sect. 3). A detailed description of the procedures followed to carry out the analysis is provided in Sects. 4, 5, 6 and 7, while Sect. 8 shows inferred results for two bistatic observations of Titan's polar regions.

2 Fundamentals of Surface Scattering

The interaction between the illuminated portion of a planet's surface and a transmitted signal is governed by very complex phenomena. Electrical properties of the ground, like the dielectric constant, describe quantitatively how a fraction of the incoming signal may be absorbed by the planet, while the reflection is driven by the induction of various scattering behaviors by the surface statistics [7].

If an incoming signal is modeled as a beam of rays, and the illuminated surface is discretized into unitary elements dS , the scattering process can be inspected at each unit surface, and the total reflection can be thought as the integral of contributions from all the illuminated unitary elements.

Figure 1 shows a point-wise surface scattering scenario. At a given point over the surface (x, y, z) , depending on the terrain's properties, for a precise incoming orientation of the signal (\hat{t}') , the power will be partially scattered in the specular direction (\hat{s}) , partially diffused more uniformly "forward" or "backward" (respectively orange and green arrows in Fig. 1) with respect to the local reflection point, and partially absorbed. Of this three dimensional scattered power field, what is received by the receiver depends on its position (\hat{r}') . The specific radar cross section σ_0 expresses the power reception as a function of reflection point over the surface, incoming and reception directions [1]:

$$\sigma_0(x, y, z, \hat{t}', \hat{r}') \quad (1)$$

The total echo power coming from a surface element can be described as:

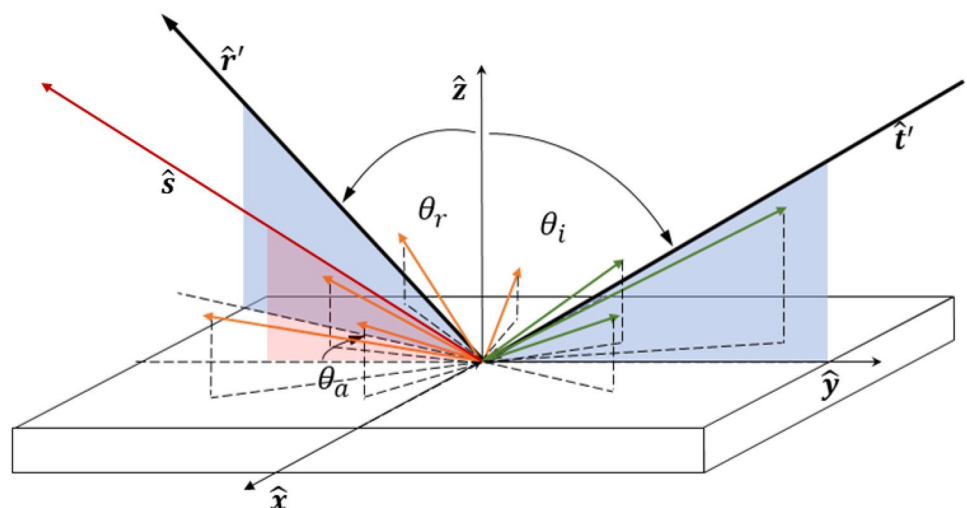
$$dP_r = \frac{P_t G_t}{4\pi |\hat{t}'|^2} \sigma_0 \frac{\lambda^2 G_r}{(4\pi)^2 |\hat{r}'|^2} dS \quad (2)$$

where P_t is the transmitted power, G_t and G_r are transmitting and receiving gains, and λ is the radar wavelength [1].

The local radar cross section of a planet is usually written combining general laws for different scattering components. The main ones with planet's surfaces are quasi-specular scattering, associated with isotropic and homogeneous smooth regions, and proportional to the surface height distribution; diffuse scattering due to more fractured or rocky terrains, and sub-surface, or volume scattering, which is abundant in icy targets [1]. The generic radar cross section for a planet's surface can be written as

$$\sigma_0 = \underbrace{\sigma_{QS}}_{\text{Quasi-specular}} + \underbrace{\sigma_D}_{\text{Diffuse}} + \underbrace{\sigma_V}_{\text{Volume}} \quad (3)$$

Fig. 1 Model of local bistatic reflection. \hat{t}' and \hat{r}' denote respectively transmitter and receiver directions, while θ_i and θ_r are incidence and reflection angle. For $\theta_i = \theta_r$, the scattering is said to be specular (\hat{s} red line). For $\theta_a = 0$, we talk about forward scattering. Orange and green arrows are shown as examples of scattering in various directions



Titan makes no exception to this [7, 8]. In [5], many observations of Titan with the ground-based Arecibo observatory and Green Bank Telescope are analyzed, revealing how echoes from the moon of Saturn are dominated by specular and diffuse scattering components. Whether the latter is mainly due to multiple subsurface scattering or superficial wavelength-scale structures, depends on the illuminated region, and can not be stated definitively [7].

3 Bistatic Radar Experiment

Despite the recent interest that the uplink and crosslink bistatic configurations are arousing, downlink geometries have been employed so far for planetary surface probing, with very few exceptions [1, 9]. From the wave propagation point of view, all the configurations are equivalent, but the higher sampling rates and more powerful computational units available in a ground-based facility make the downlink one simpler to implement, despite the promising higher sensitivity of uplink experiments [10].

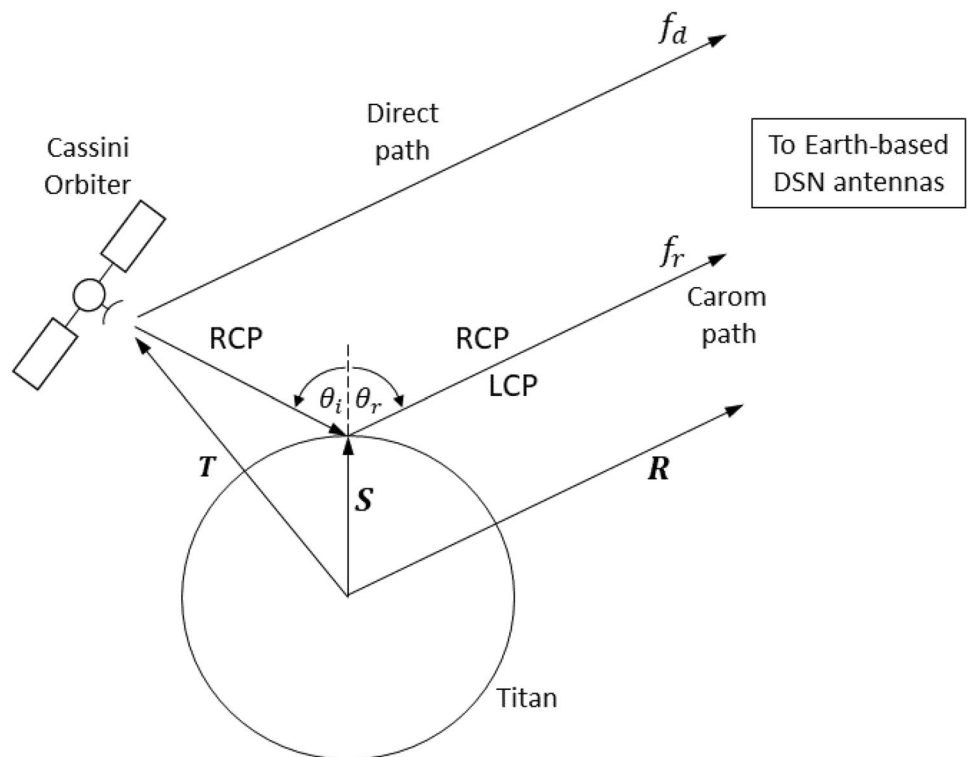
Figure 2 depicts the geometry of a generic downlink bistatic experiment carried out by Cassini. The radio link of the observation consists of an unmodulated radio signal, sent with right-sense circular polarization (RCP), that reaches Earth through a scattered path (Carom path in Fig. 2) made of two segments separated by a specular point (*s* in Fig. 2). After the reflection, two orthogonally left-sense

and right-sense circularly polarized components (LCP and RCP) of the signal leaves Titan. A side-lobe “direct path” from the probe may reach the ground as well, and it would be affected by a Doppler shift different from the one of the scattered path [11].

As explained in Sect. 2, electrical properties and roughness of the surface determine the three dimensional scattering of signal power, while the bistatic experiment geometry, constrained by the relative positions of Titan, Cassini, Earth and by Cassini’s antenna orientation, defines which fraction of the reflected echoes will reach the receiver. Referencing again to Fig. 2, when a radio link lying on a single plane has incidence (θ_i) and reflection (θ_r) angles almost equal too each other, the observation is said to be quasi-specular and near-forward.

Fjeldbo provided the theoretical foundation of the quasi-specular bistatic experiment to probe planetary surfaces in [12], applying a physical optics model to analyze the scattering process from a moderately rough surface: the Kirchoff Approximation (KA). If (1) homogeneous and isotropic, (2) with a radius of curvature greater than the radio wavelength λ , (3) a correlation length larger than the wavelength and 4) negligible subsurface scattering, the reflecting surface can be modeled with a facet-based grid of large scale tiles ($\gg \lambda$ in size) behaving as infinite planes, and the major contribution to the echoes arises from specular forward reflections from these mirror-like surface facets [1]. Each facet is tilted with respect to the planet’s mean surface, and has

Fig. 2 Cassini downlink bistatic experiment geometry. The transmitted signal is right circularly polarized (RCP). Its reflection, made of orthogonally polarized components (RCP, LCP), lies on the same plane as the incoming signal (near-forward), and $\theta_i \approx \theta_r$ (quasi-specular)



an horizontal scale of dimensions between few tens to few hundreds of radar wavelengths, with an effective size being on the order of 200λ [13]. A precise determination of the horizontal scales to which estimates of surface properties apply, and conditions under which the Fjeldbo model breaks down or need corrections, remain an active field of research today [10]. Echoes are then affected by how many facets are tilted in the right direction for a specular reflection towards the receiver, and on the surface dielectric constant, responsible for the incoming power distribution among absorption, reflection and polarization. Since the rms surface slope is the adirectional average tilting of these large scale tiles over the the reflecting surface, it should be understandable, at least in principle, how rms surface slope and dielectric constant affect the received echoes.

Fjeldbo's results, used here to analyze Cassini bistatic radar data, were derived under the assumptions of small incidence angles ($\theta_i < 60^\circ$) and full illumination of the planet's surface [12]. The validity of his model for larger incidence angles has been proven, at least for the Moon, and here, as Simpson and Tyler did in their preliminary analysis of the Viking bistatic radar data for Mars [14], the model is assumed to work despite larger incidence angles. The application of Fjeldbo's model to orbiter-based observations where the antenna footprint illuminates a limited region of the planet is not new. In practice, there is an effective scattering region around the specular point which is responsible for most of the quasi-specular echo and is proportional to the rms surface slope [10]. A rough surface enlarges this area, and, if the illuminated region is too narrow, the broadening estimates will mimic the antenna pattern rather

than the scattering processes of the surface [1]. In these scenarios, a bistatic radar observation is said to be "beam-limited", and some corrections should be applied. This problem was not an issue during the bistatic observations analyzed here because of the general smoothness of illuminated terrains.

3.1 Surface Roughness

While the spacecraft, the receiving antenna and the target planet itself are moving, the fraction of the signal travelling via the specular point undergoes a Doppler shift:

$$f_s = -\frac{1}{\lambda} \frac{d}{dt} \{|\mathbf{r}'| + |\mathbf{t}'|\} \quad (4)$$

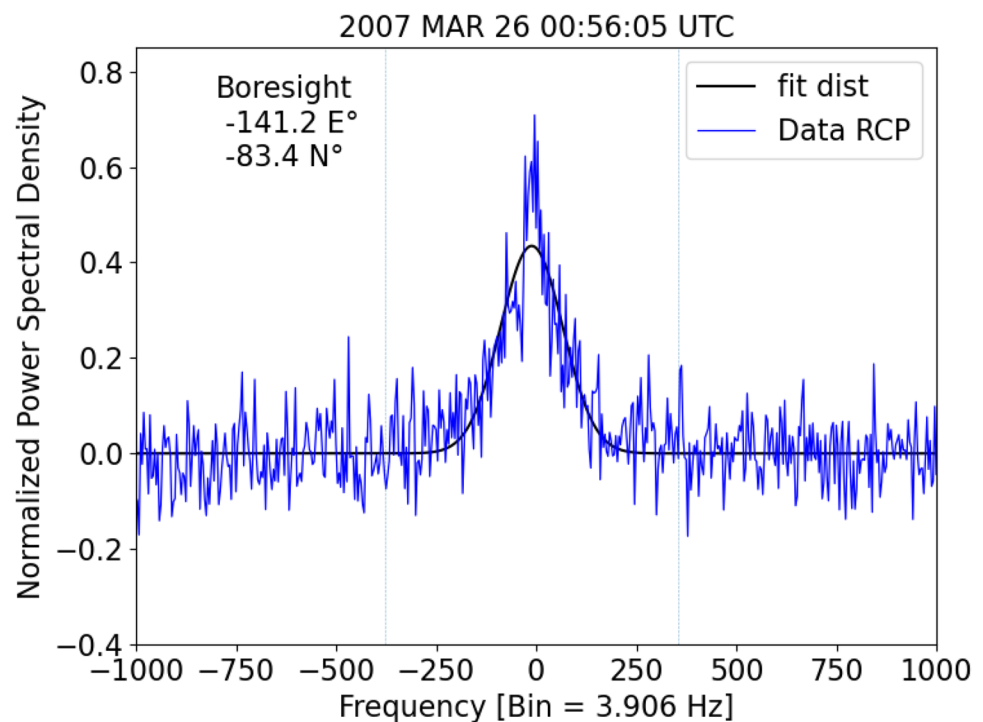
where \mathbf{r}' and \mathbf{t}' are receiver and transmitter positions with respect to the specular point. Different illuminated scattering locations around the specular point are responsible for power contributions differently shifted in frequency. This results in a spectral broadening of the echo signal. The power spectrum of the echo has a bell shape whose central peak corresponds to the downlink carrier frequency shifted by the Doppler at the specular point [1] (Fig. 3).

In the meantime, the side-lobe direct signal is Doppler shifted as well:

$$f_d = \frac{1}{\lambda} \frac{d}{dt} \{|\mathbf{r} - \mathbf{t}|\} \quad (5)$$

and a second isolated peak may become visible in the spectrum. If the differential Doppler shift between direct and

Fig. 3 Example of normalized power spectral density of echoes received during the bistatic ingress observation of flyby T27. Cassini HGA boresight intersection with Titan's surface and observation time are labelled. The spectrum peak is centered close to zero thanks to the accurate tracking of the sky frequency by the Radio Science Receiver. The two vertical lines denote an interval four times the half-maximum full-width of the Gaussian template fitting the spectrum



scattered path $|f_d - f_s|$ is large, which is likely for fast spacecrafts, huge target bodies and incidence angles far from 90° , direct peak and broadened echo portion of the spectrum may be far away from each other [15]. This is the case for Cassini, where the differential Doppler is in the order of hundreds of kHz, and this is the reason why the direct side-lobe does not appear inside the 16 kHz reception bandwidth selected for the following analysis.

For a planetary surface with a Gaussian height distribution, the half-power bandwidth (B) of the echo spectrum can be related to the rms surface slope by the following formula:

$$B = 4\sqrt{\ln 2} \left(V_s \frac{\zeta}{\lambda} \right) \cos \theta \tag{6}$$

where ζ is the rms surface slope in radians, V_s is the specular point velocity across the planet surface, and θ is the specular angle [1]. Incidence angle and velocity of the specular point are quantities related to the geometry of the problem, and the rms slope can be extracted from the echoes' spectra through Eq. (6).

The concept of rms surface slope drives the quasi-specular reflection process, and describes the average adirectional tilting of smooth facets with an effective size of around 200λ in which the illuminated surface can be discretized [14]. The presence of diffuse and subsurface scattering due to surface features equal or smaller than the radar wavelength [16] is not consistent with the KA model, but may characterize echoes from the surface of Titan [7]. To be consistent with the theoretical foundation of the approach followed here, signal contributions from different scattering mechanisms should be separated, so that the broadening fed to Eq. (6) results from specular scattering only. Ideas involving the computation of the coherency matrix of the orthogonally polarized components of the reflections to distinguish between diffuse and specular echoes have been proposed [2, 17], but the issue is not tackled in this first-order analysis.

3.2 Dielectric Constant

A polarized incident signal that reaches a planar interface between free space and a planetary surface generates a reflected wave made of two components polarized in two orthogonal ways. The amplitude of the two polarized parts of the scattered signal is described by the Fresnel voltage reflection coefficients, which are related to the dielectric constant (ϵ) of the scattering surface and to the specular angle (θ) of the bistatic geometry [1]. For a linear polarization we have

$$R_{HH} = \frac{\cos \theta - \sqrt{\epsilon - \sin^2 \theta}}{\cos \theta + \sqrt{\epsilon - \sin^2 \theta}} \tag{7}$$

$$R_{VV} = \frac{\epsilon \cos \theta - \sqrt{\epsilon - \sin^2 \theta}}{\epsilon \cos \theta + \sqrt{\epsilon - \sin^2 \theta}} \tag{8}$$

Cassini transmitted circularly polarized signals with a right-sense circular polarization. Fresnel coefficients for circularly polarized waves are the following:

$$R_{SC} = \frac{(R_{VV} + R_{HH})}{2} \tag{9}$$

$$R_{OC} = \frac{(R_{VV} - R_{HH})}{2} \tag{10}$$

where R_{SC} is the voltage reflection coefficient for the same sense circular polarization as the one of the transmitted signal (RCP). R_{OC} means opposite sense circular polarization (LCP) [11].

To compute the surface dielectric constant, it is possible to work separately on the two polarizations measuring the orthogonally polarized echo powers, and going for the computation of the surface reflectivity $\eta(\theta)$, but it is easier to work on the ratio between RCP and LCP echoes' strength.

$$\frac{P_{SC}}{P_{OC}} = \frac{P_{RCP}}{P_{LCP}} = \frac{\eta_{SC}}{\eta_{OC}} = \frac{|R_{SC}|^2}{|R_{OC}|^2} \tag{11}$$

Once the power ratio is measured, by solving the system of equations from (7) to (11), the dielectric constant of the surface material can be assessed. As for the rms slope, diffuse components of the echoes should be removed from the computation of the polarized reflected power, but this was not taken into account [2].

Table 1 provides a list of materials that are likely to be found on Titan, and their expected relative dielectric constants.

For any of them, the incidence angle that brings the power ratio between circularly polarized components to unity is the Brewster angle. For incidence angles close to 90° , power ratios get very large, and a lower signal-to-noise ratio for the weaker polarized component increases the unreliability

Table 1 Dielectric constant and loss tangent of possible materials of Titan's surface [18]

Material	Dielectric constant	Loss tangent
Liquid hydrocarbons	1.6–1.9	$< 10^{-5}$
Solid hydrocarbons	2.0–2.4	$\sim 10^{-4}$
CO ₂ ice	2.2	< 0.005
Water ice	3.1	$2 * 10^{-5}$
Water-ammonia ice	4.5	0.01
Organic heteropolymers	4.5–5.5	$< 10^{-5}$
Meteoritic material	8.6	0.9

of the total reflected power computation [2]. The Brewster angles of various materials on Titan lie in the range 51–65° [19], and observations at incidence angles out of this window may produce deceptive dielectric constant values.

If the surface material is conducting, its dielectric constant is a complex number. This opens up to a set of electrical properties of a material, like conductivity, penetration depth and loss tangent $\tan \delta$, which is the ratio between imaginary and real part of ϵ [2], that could enrich the current understanding of Titan's surface and sub-surface. In [20], Paillou measured dielectric constant, loss tangent and penetration depth through Ku-band observations of Titan's surface materials, reproducing them in a lab. His results are consistent with Table 1, but he expanded on those taking the materials conductivity into account. Inferred imaginary parts are in the order of 10^{-3} . Two types of compacted tholins are exceptions, with values in the order of 10^{-2} . These two are highly conductive materials with low backscatter [20].

For this work, Titan's materials are assumed slightly lossy dielectric, with a real dielectric constant. Conductivity and penetration depths are not computed. This choice is motivated by the preliminary role played by this data analysis.

4 Geometry of the Experiment

Cassini performed bistatic radar observations during 13 Titan's flybys, sometimes in conjunction with radio science occultation experiments. The spacecraft HGA illuminated equatorial, mid-latitude and polar regions of the saturnian satellite with right circularly polarized signals transmitted in three frequency bands (table 2). For each observation, the trajectory and antenna pointing of Cassini around the flyby of interest, as well as the positions of Titan and receiving DSN stations, were modeled with the help of the SPICE toolkit, distributed by the NASA Navigation and Ancillary Information Facility (NAIF).

The theoretical specular point location is unique and fixed, as soon as the transmitter, receiver, barycenter and shape of Titan are defined. The numerical routine to locate it is explained in detail in Appendix 1. Incidence angle and

specular point velocity were computed as well for later processing.

During bistatic observations, the spacecraft is continuously maneuvered to point its antenna to the theoretical specular point. The consequences of bad pointing may be a reduction of power received on Earth, or a changing in the portion of illuminated surface. Values of pointing error are always more than ten times smaller than the half-power half-beamwidth of the antenna, at least in S- and X- bands. This level of error is expected to have a small effect, and it is not considered in the following [14].

5 Signal Processing

For this analysis, the X-band signals were chosen because of their highest signal-to-noise ratio. S-band has the largest half-power beamwidth, and this makes the physical interpretation of Titan's terrains properties harder, because inferred surface properties are averaged over a larger total illuminated surface. The Ka-band has the lowest half-power beamwidth, hence increasing the chance of beam-limitation.

Signals from Cassini, in different bands and polarizations, were down converted and digitized by different Radio Science Receivers inside the DSN complexes. Raw data are collected with sampling frequency of 16 kHz as sequences of complex samples made of an in-phase (I) component and of a quadrature (Q) component. For the processing of raw data the periodogram technique was used. The power spectral density of short subsets of 4096 samples (0.256 s of integration time) was computed, and a combination of time and frequency averaging was later performed to reduce the variance of the spectral estimation. The count time is the final time resolution of the spectra. For example, an integration time of 0.256 s, combined with a time averaging over 240 spectra, produces a final array of spectra with count time 61.44 s. Averaging comes with the price of a resolution loss, which is not desirable. With a low time resolution, characterizing a limited illuminated region of Titan becomes harder, since features of a broader area are averaged in a single output. For smooth surfaces, the broadening may be very narrow, and an overestimation of the actual roughness may occur if the half-power bandwidth is in the order of a single frequency bin [14]. The best trade-off between coherent and incoherent integration was found taking these issues into account, and targeting a high signal-to-noise ratio.

6 Inference of Surface rms Slope

Once the spectra are processed, the inference of the rms surface slope requires an estimation of the spectral broadening. Each power spectral density was fit with a proper template,

Table 2 Cassini Radio Science Subsystem operating frequency values. The half-power beamwidth is the angular opening of the antenna main lobe where the radiated power goes below 3dB [21]

Band	Uplink [GHz]	Downlink [GHz]	HP Beamwidth
S	N/A	2.298	2.125
X	7.175	8.425	0.635
Ka	34.316	32.028	0.167
Ku	13.776	13.800	N/A

and the full-width half-maximum of the fitting curve was extracted. A Gaussian template was chosen for mathematical convenience, since past experience suggests that echo shapes usually deviate somewhat from the Gaussian, but for a first-order analysis Gaussian fitting can be considered satisfactory [14, 22, 23].

The main weaknesses of the fitting performance of a Gaussian curve are shown in Fig. 4: low tails near the base of a spectrum, very narrow and high peaks and asymmetrical echoes from heterogeneous surfaces [14]. A strong and sharp peak at the center of the spectrum has been quite of a recurring feature in the inspected bistatic radar observations, due to the presence of stable bodies of liquid hydrocarbons in the northern pole of Titan, responsible for an almost negligible spectral broadening, low rms slopes and strong reflection amplitudes.

In general, a spectrum with a strong and sharp peak surrounded by a lower and broader base is explained with the presence of a smooth inclusion within a moderately rough reflecting area [14]. For Titan, such an echo may arise from liquid bodies surrounded by rougher shores falling inside the illuminated and the effective area. The lack of a proper separation between diffuse and quasi-specular echoes introduces an ambiguity about the lower tails of the spectrum, that may be part of the diffuse scattering from fractures and boulders or specular echoes from rougher regions, like rims or shores.

As shown in the 3rd and 4th plot of Fig. 4, the incredibly narrow peaks from Titan's Maria represented unprecedented spectra to be fitted among echoes from planetary surfaces. The Gaussian fit failed to go for the actual peak for the majority of echoes from liquid bodies, making the surface roughness of the large seas undetectable. To study

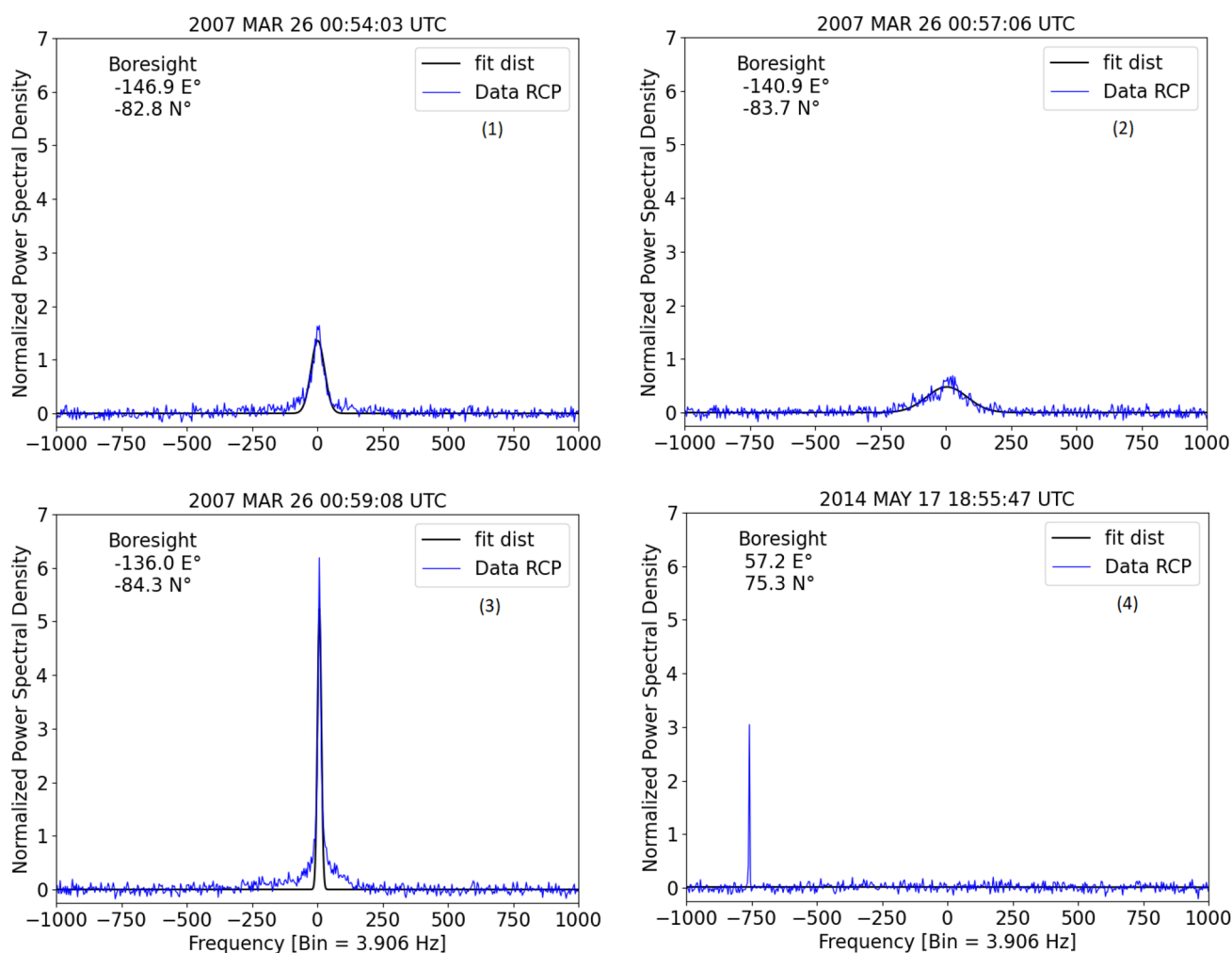


Fig. 4 Example of Gaussian fit performance on Titan's echoes. Signals have been normalized by the noise baseline, and the noise pedestal was removed. (1) Overall good fitting performance, but the asymmetry at the base of the spectrum is not fitted. (2) Example of

good fit of echoes from moderately rough surfaces. (3) Poor fitting curve missing the lower tails of a strong central spike. (4) Example of Gaussian curve missing a very strong a narrow peak when applied to echoes from Kraken Mare

the sea-related flybys, the fitting function was weighted at the peak, forcing the Gaussian curve to pass through it.

Since surface roughness does not depend on the polarized component in analysis, the same value of rms slope should be obtained from the analysis of both the LCP and the RCP components of the reflected echoes. In practice, the two orthogonal portions of the signal had different signal-to-noise ratios because of the high values of incidence angle of observation [2]. Hence, it was convenient to work on the stronger right circularly polarized component only, to fit the spectrum, estimate the half-power bandwidth and compute the rms surface slope. This is not the first time this approach is used to estimate surface roughness from orthogonally polarized signal components of different strength [24].

7 Inference of Dielectric Constant

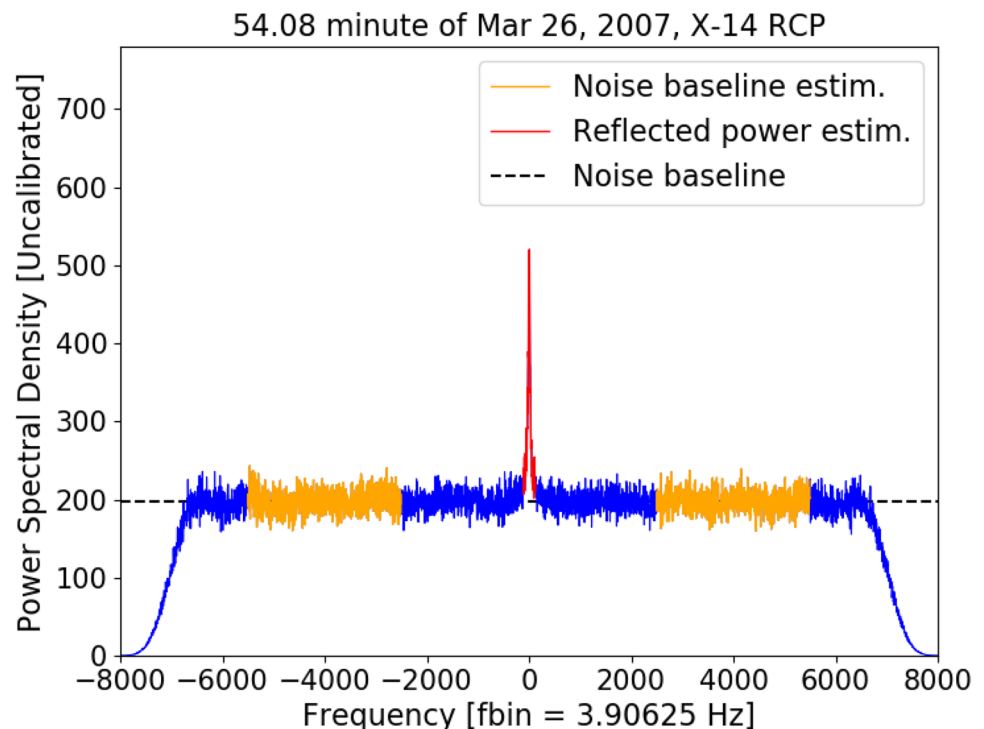
For the computation of surface dielectric constant ϵ , the power ratio between RCP and LCP reflected components must be fed to the nonlinear system of equations from (7) to (11). For each polarization, the reflected power was computed as a difference between received power and noise power, both evaluated within a “useful” integration bandwidth. We summed the power spectral density samples within the useful bandwidth times the frequency bin for the received power, while the noise power was computed as the product between noise density baseline N_0 and useful integration bandwidth.

For the noise baseline estimation, an average of the behavior of the power spectral density over a series of bands of growing width from 1 to 3 kHz, step of 50 Hz, and centered at ± 4 kHz was performed (Fig. 5). Later, the different noise baseline estimates were averaged again, and eventually left and right-hand side estimates of N_0 were averaged to obtain a single, robust value of uncalibrated noise power density.

The useful integration bandwidth was chosen according to [14]. A band centered at the Gaussian peak f_p was defined as $f_p \pm 2\Delta f$, with Δf half-power bandwidth of the RCP spectrum successfully fitted with the Gaussian template (Fig. 5). The only constrain to this was that the band could not be shorter than 15 or larger than 150 frequency bins [14]. When the Gaussian fit was unsuccessful, even for the stronger RCP component, we considered the reflection to be too noisy to estimate the dielectric constant.

What reaches the ground is amplified by the open-loop receivers before processing, and the amplification could be different for the two polarizations [25]. To avoid overestimation or underestimation of the ratio between orthogonally polarized reflected powers, due to different amplifying gains, an absolute amplitude calibration of the recorded digital samples is required. The system noise temperature T_{sys} has to be measured throughout the observation, to later compute the amplification gain between actual noise power density $N_0 = kT_{sys}$, where k is the Boltzmann constant, and the noise baseline of the signal at the receiver output, which is amplified. In principle, measurements of system noise temperature

Fig. 5 Uncalibrated spectrum of a signal received during flyby T27. The bands for noise baseline estimation are highlighted in orange, while the red portion spans over the useful band for reflected power computation. The estimated noise density baseline is highlighted with an horizontal dashed black line



can be gathered from the analysis of pre-calibration, post-calibration and mini-calibrations performed during Titan's flyby [26, 27]. For this first-order work, it was assumed that the noise temperature was the same for LCP and RCP received components, hence performing a relative calibration between polarizations.

8 Result of Data Analysis

8.1 Flyby T101: Titan's Northern Seas

Flyby T101 is the first ever scenario of bistatic reflections from two of the polar seas of Titan: Ligeia and Kraken Mare. Inspected signals are X-band LCP and RCP components of echoes received by the 70-meter antenna DSS-43 in Canberra.

The ground track of the specular point during the bistatic egress observation of flyby T101 is shown on the left in Fig. 6, where it can be seen how the HGA footprint illuminates two main types of terrain. The plot of the signal peak-to-noise ratio, provided on the right in Fig. 6, shows a clear difference in the scattering behavior of dry lands versus stable liquid bodies. After Ligeia shores, which are close to location 2 in Fig. 6, the antenna footprint covers a dry region, and the peak-to-noise ratio drops fast before and after Moray Sinus: an estuary located at the northern end of Kraken Mare [28].

In Fig. 6, the half-power beamwidth footprints, which can be considered average illuminated areas [1], are highlighted over Titan around the four numbered locations of interest.

Within such large regions, what effectively characterizes the shape of the echoes, are the effective areas surrounding the specular point, introduced in section 6 and function of surface roughness. Over the incredibly smooth seas, the effective reflecting regions are of sizes from few tens of km² up to few hundreds of km² towards the end of the observation. Each punctual output of surface roughness and relative dielectric constant is extracted from a single spectrum averaging the properties of what's covered by the effective area around the moving specular point within a count time (Fig. 7). Such a small effective area of reflection justifies why, despite the large antenna footprint illuminating both liquid and dry surfaces at the same time, the peak-to-noise ratio is very sensitive to the specular point position (Fig. 6).

In Fig. 8, spectra of received echoes in both polarizations from the four locations highlighted in Fig. 6 are presented. Each spectrum is made of 4096 bins of 3.90625 Hz, and results from a choice of 0.256 s of integration time and time averaging between 240 spectra, for a total time resolution of approximately one spectrum per minute.

Echoes from locations 1 and 4 are consistent with Titan's seas being highly reflective and smooth. The slightly broader echoes from location 1 could descend from Fjeldbo equation, inverted and written below.

$$\zeta = \frac{B\lambda}{4\sqrt{\ln 2}(V_s \cos \theta)} \tag{12}$$

For a given rms slope, the broadening grows with the product of specular point velocity and cosine of the incident angle. Throughout this bistatic egress observation, the

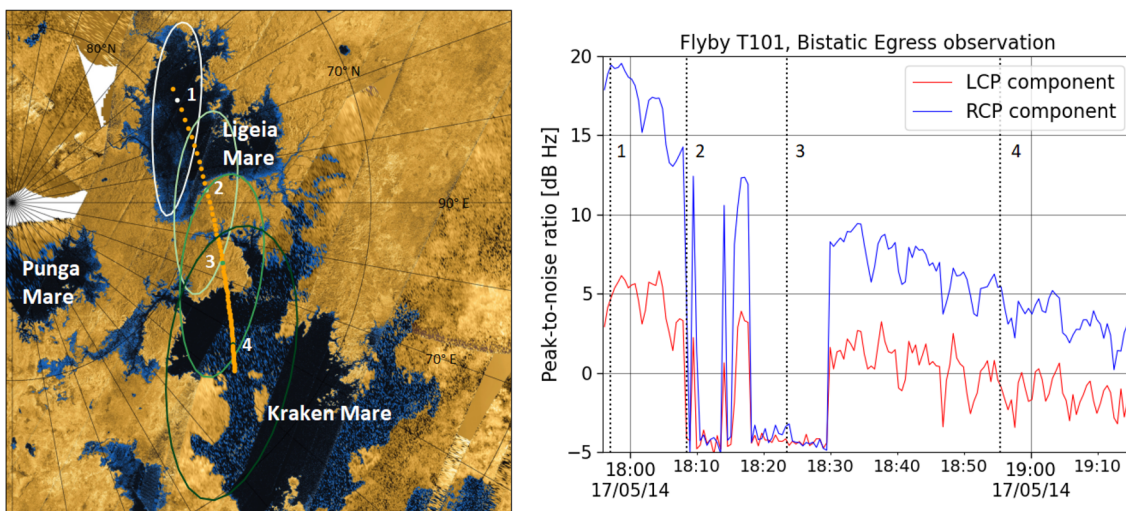


Fig. 6 Left: Specular point track of the bistatic egress phase of flyby T101 spanning over the northern pole of Titan. Four locations of interest are labelled for further discussion. The footprint of the X-band half-power beamwidth is drawn, and it enlarges from ≈40,000

to ≈200,000 km² as Cassini flies away from Titan. Right: Uncalibrated signal peak-to-noise ratio during the observation for X-band LCP and RCP components. The four points highlighted on the left are labelled here as well

Fig. 7 Detail of the effective area size for a portion of Ligeia Mare close to location 1 from Fig. 6. A trail of white markers draws a specular point track with 2.048 s of resolution. The white ellipses are the respective effective areas along the track. The red markers coincide with the yellow dots from the specular point track of Fig. 6, resolution equal to the processing count time: 61.44 s. Each value of rms slope or dielectric constant, which is associated to a reflecting region centered at each red dot, averages what happens in the set of effective areas grouped by a curly bracket



specular point slows down over the surface of Titan more than the cosine of the incidence angle grows, and this justifies a reduction of the inferred broadening. The decreasing strength of reflection is due to the growing altitude of the spacecraft over Titan's surface.

Point 2 in Fig. 8 shows echoes from the shores of Ligeia Mare. There is still a patch of smooth and liquid surface around the specular point, but a barely visible plateau of diffusive echoes appears at the base of the peak. Ligeia shores may be smooth but covered by boulders and rocks, or heavily fractured, and not responsible for a quasi-specular reflection.

The effective illuminated patch of terrain at location 3 should be completely dry, and the broadening is the largest of the entire observation. It is hard to confidently state whether these dry echoes are diffusive or very weak quasi-specular ones.

8.1.1 Roughness

Figure 9 shows the rms surface slope profile throughout the observation. From a relative standpoint, Ligeia Mare appears rougher than Kraken Mare. The spectral broadening found for liquid bodies is very close to the size of a single frequency bin, which could imply a broadening overestimation due to the low frequency resolution of the processed spectra. In [14], Simpson suggests that rms values from Viking inspection of Mars surface could be considered reliable when the echo width is approximately equal to at least 7 frequency bins. Hence, it would be correct to consider the values of surface slope proposed here as upper bounds.

The roughest patch of terrain seems to be location 3 in Fig. 6, with $\zeta = 0.35^\circ$, which is a very low value compared to measurements gathered for other dry planetary surfaces, like Mars [14] or the Moon [24]. Yet, slopes as low as 0.3° were found also from Arecibo observations of Titan [5].

We found the seas to be extremely smooth, which is consistent with [29], with $\zeta \approx 0.017^\circ - 0.035^\circ$ for Ligeia Mare and $\zeta \approx 0.040^\circ - 0.1^\circ$ for Kraken Mare. Computed values should be considered upper bounds, and they are almost two orders of magnitude lower than Grima's results from RADAR data analysis [6], who estimated Ligeia and Kraken Mare roughnesses around $1.1^\circ - 1.7^\circ$ and $1.6^\circ - 2.4^\circ$ respectively. As mentioned in [6], Stephan's analysis of 2009 VIMS observations produced values of 0.15° as upper bounds for Kraken's surface roughness, suggesting a completely smooth surface with no waves [30]. Grima's observations were carried out during the same time window of flyby T101, and bistatic radar data agrees with RADAR observations on the fact that Ligeia Mare is, on average, smoother than Kraken Mare [6].

Bistatic radar experiments carried out over Earth's seas yielded rms slopes of 0.03° with winds of 5 m/s [31, 32]. Entering the northern spring of Titan, winds of $0.4 - 0.7$ m/s are expected to ripple Titan's seas, leading to the possible formation of capillary waves, as explained by Hayes in [33]. The rms slope shown in Fig. 9 is not perfectly uniform, but has an oscillating trend consistent with the one of the peak-to-noise ratio. This could be the result of the illumination of patches of liquid surface of variable roughness, which could be interpreted as waves.

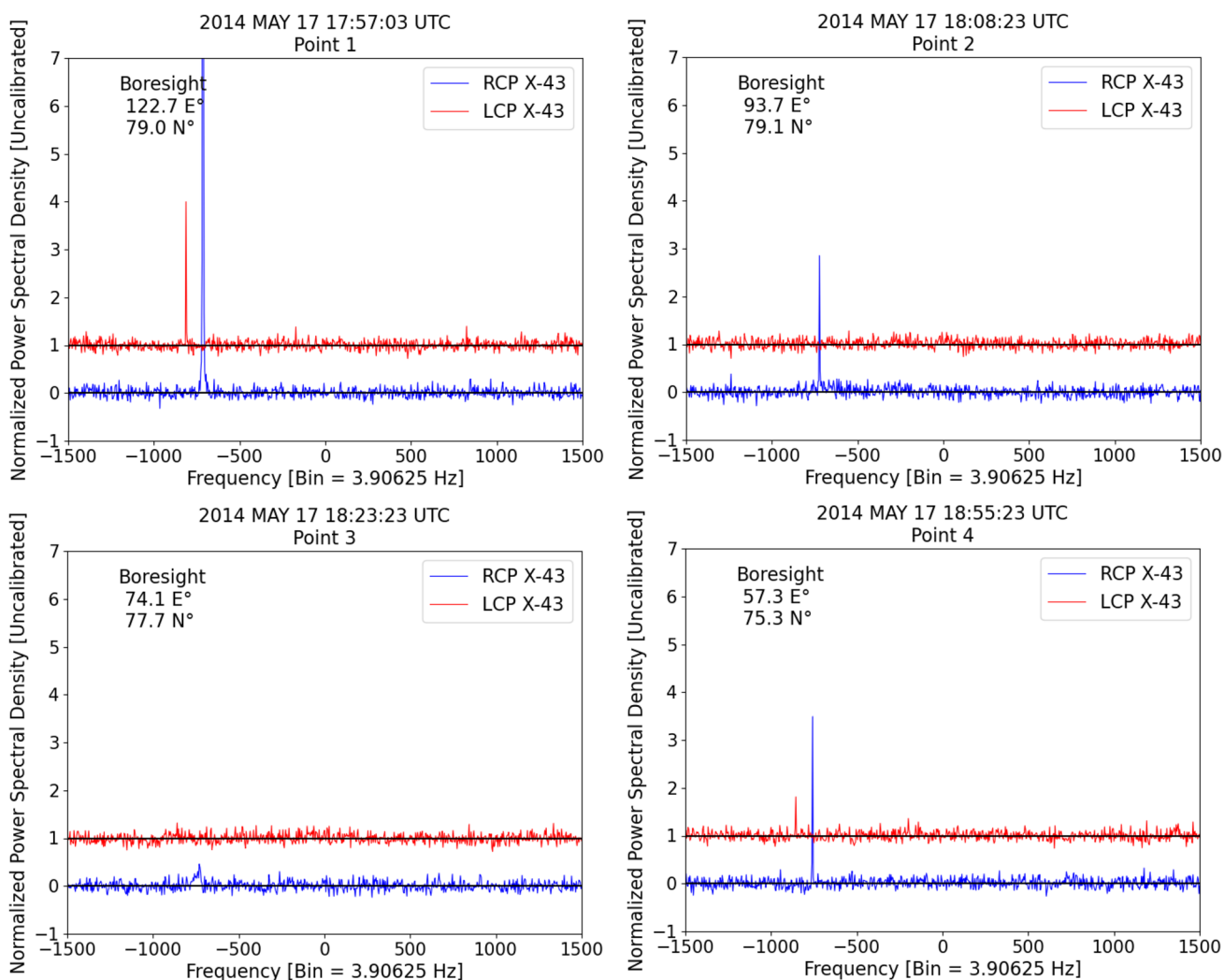


Fig. 8 X-band LCP and RCP components of echoes from locations 1, 2, 3 and 4 highlighted in Fig. 6 received at station DSS-43. Each spectrum is normalized over the noise baseline, and displaced horizontally and vertically for clarity purpose. The peak position over the frequency domain of the two polarizations should be the same.

The LCP peak is displaced, while the RCP peak is in its true position, which is around -750 Hz because of the failure of Cassini's Ultra Stable Oscillator. The Cassini's HGA boresight intersection with Titan's surface for each couple of spectra is also highlighted

8.1.2 Dielectric Constants

Values of dielectric constant are shown in Fig. 10. The reflected power computation works over very thin integration bandwidths, and may remove autonomously a portion of diffusive reflection, if present. The general scattering of the dots, especially over Kraken Mare, is most likely related to the low resolution in frequency of the spectra. Since the broadening is almost equal to the frequency bin, the reflected power computation results from the sum of very few points of the spectrum (3–4). This makes the computation very sensitive to the behavior of each individual sample, which is driven by the noisiness of the signal. We are confident that a reduction in the frequency bin size will reduce the scattering.

Liquid bodies on Titan are believed to be a dominant mixture of ethane ($\epsilon \approx 2.0$) and methane ($\epsilon \approx 1.73$), with possible traces of soluble nitrogen ($\epsilon \approx 1.5$) [6]. The average values of dielectric constant throughout the observations are $\epsilon = 1.43$ for Ligeia and $\epsilon = 1.48$ for Kraken, which are low compared to the expected results for liquid hydrocarbons. The reason behind this bias could be the lack of a proper absolute calibration of the orthogonally polarized components.

8.2 Flyby T27: Southern Pole of Titan

The bistatic ingress phase of flyby T27 spans over a portion of the southern pole of Titan. This time, the specular point ground track (Fig. 11) does not touch any stable liquid

Fig. 9 Surface rms slope in degrees against time, latitude and longitude of the antenna boresight intersection with Titan's surface. Values of surface roughness are inferred from the RCP component of the echoes

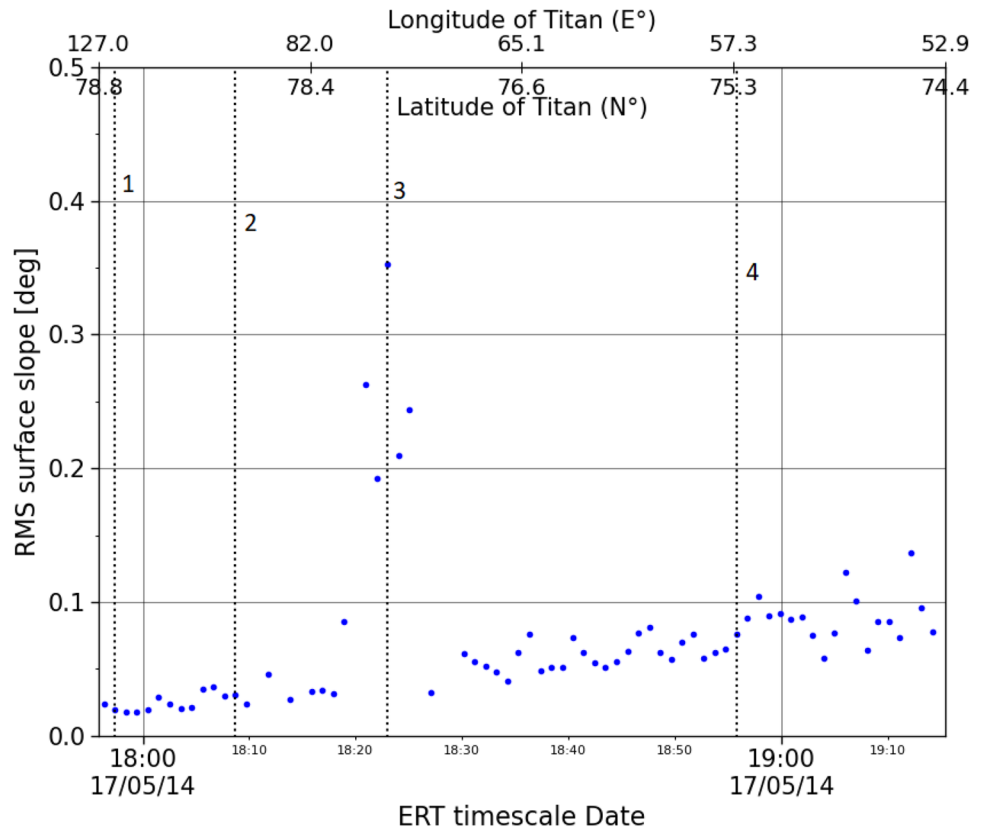
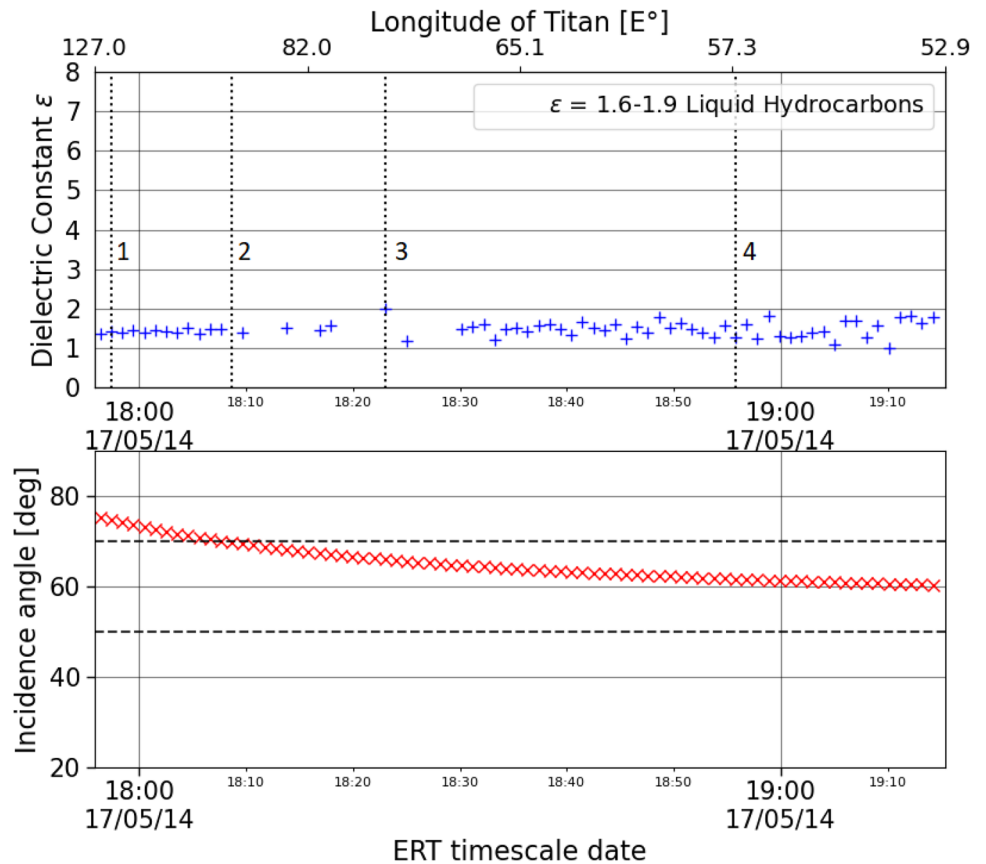


Fig. 10 Dielectric constants and incidence angles of observation against time and longitude of Cassini's HGA boresight intersection with Titan's surface. Typical dielectric constant values for liquid hydrocarbons are recalled in the legend



body, and illumination of dry terrains only is expected. It is also true that Titan's South pole should be covered by small basins sometimes filled by liquid hydrocarbons [34].

For this bistatic observation, X-band signals received at DSS-14, Goldstone, were chosen to carry out the analysis, and signal processing was performed again with 0.256 s of integration time, averaging over 120 spectra and frequency bins of 3.90625 Hz. Echoes' spectra are available each 30.72 s, and the ones received from the locations highlighted along the specular point track in Fig. 11 are shown in Fig. 12. Analogous considerations to T101 should be made for T27 about effective areas shaping received echoes. This time rms slopes are higher than the seas' ones. Still, beam-limitation should not be an issue, since the illuminated areas are always larger than the effective ones, in general smaller than 20,000 km².

Locations 1 and 3 are particularly interesting, since their spectra are reminiscent of northern pole reflections from Titan's seas. Echoes are in both cases narrow and strong in amplitude, but with a larger broadened base with an asymmetrical shape. The presence of a broad base is a sign of rougher terrain around a highly smooth and reflecting patch of land that produces such a slim central spike. A reasonable guess could be that Cassini's HGA boresight, in locations 1 and 3, is illuminating the liquid surface of basins filled with liquid hydrocarbons.

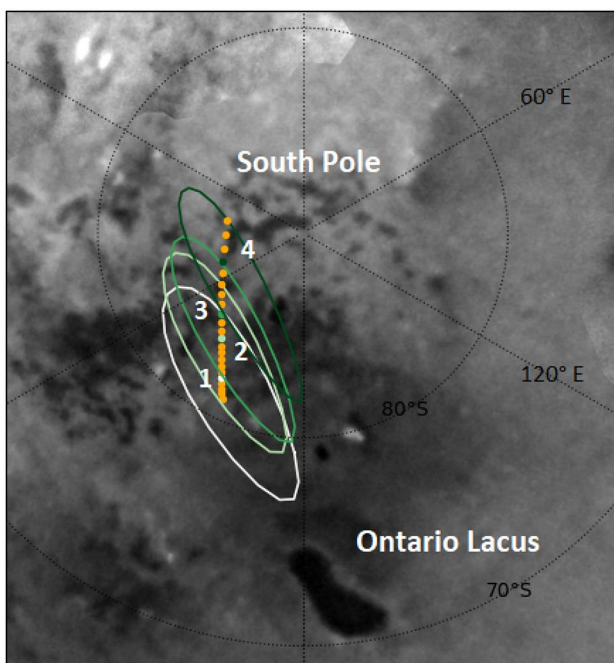


Fig. 11 Specular point track of the bistatic ingress phase of flyby T27 spanning over the southern pole of Titan. Four locations of interest are labelled for further discussion. The X-band half-power beamwidth footprint is shown, and it shrinks from $\approx 80,000$ to $\approx 40,000$ km²

Location 2 is the roughest patch of land of the observation, and its echoes have a quasi-specular appearance, differently from what happens at point 4. In location 4, the roughness is close to the one inferred for location 2, but the spectrum has the typical signature of diffuse scattering, with no specular reflection. Moving northern along the specular point ground track, the situation does not improve, and an increasingly broader diffuse scattering seems to dominate echoes, hinting at a fractured or dissected surface far from the gently undulating model. Another possible reason for this loss of quasi-specular reflection, could be the incidence angle increasing towards 90°, and the potential effect of shadowing [35].

8.2.1 Roughness

A plot of the inferred rms surface slope each 30.72 s shows low values of roughness for the southern pole track covered by Cassini's boresight during this observation (Fig. 13). Values oscillate from 0.9° down to 0.5°, to rise again up to 1.38° and fall back to 0.5° before the loss of quasi-specular reflections. The growing values of rms slope towards the end of the observation are due to the fitting of the weak and broad diffusive echoes by the Gaussian curve, which means that we should not consider them to be meaningful. From point 4, the quasi-specular bistatic observation is not suitable anymore to probe the planetary surface.

Locations 1 and 3 have rms slopes in the order of 0.1° – 0.15°, which is a familiar result, and reinforces the interpretation of echoes from these regions to be echoes from stable liquid bodies. Of the two, the basin in location 3 may be larger, because of the three consecutive low values of rms slope.

8.2.2 Dielectric Constant

Figure 14 shows dielectric constant values scattering between solid hydrocarbons and water ice, which are the most abundant materials over Titan's surface [34]. The profile found is quite smooth and does not show relevant discontinuities, which is a promising fact. Inferred numbers suggest an higher presence of water ice between locations 2 and 3 compared for example with the chunk of land before location 2, where solid hydrocarbons seems more present. Interestingly enough, around location 3, we have few estimates below $\epsilon = 2.0$, hinting at the presence of liquid hydrocarbons within the illuminated region. It is not the case for location 1, and the reason could be the smaller size of the first basin, occupying only a small portion of the illuminated area.

Large incidence angles, responsible for very weak LCP components, do not set up an ideal framework for surface electrical properties computation. We do not consider the

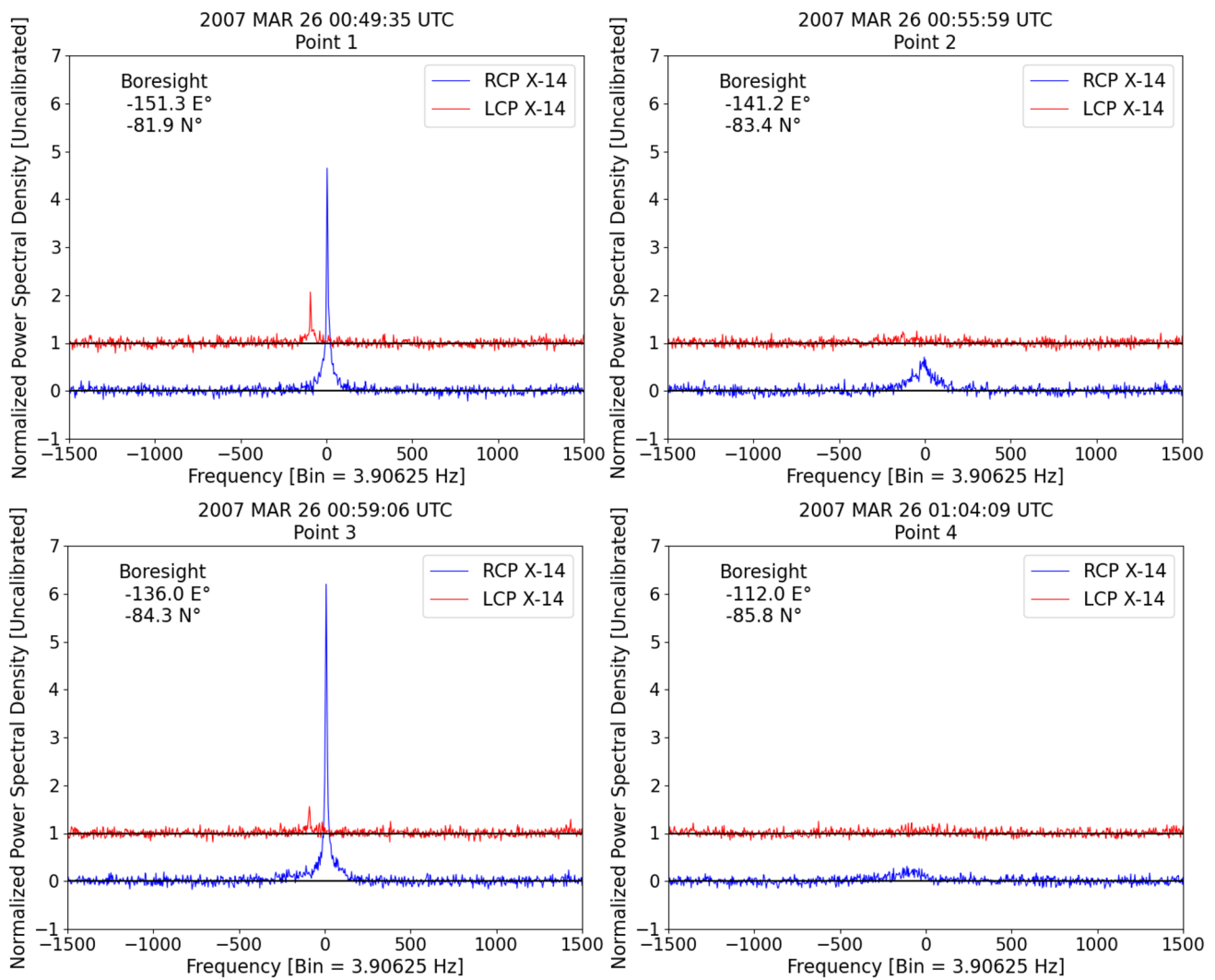


Fig. 12 X-band LCP and RCP components of echoes received at station DSS-14 from locations 1, 2, 3 and 4 highlighted in Fig. 6. Each spectrum is normalized over the noise baseline, and displaced

values of dielectric constant inferred towards the end of the observation to be meaningful, since the scattered power is not related to quasi-specular echoes anymore, and shadowing may come into play.

9 Conclusions and future work

The initial goal of this work was to approach from scratch a radio science experiment with a few related literature data, trying to understand its basic principles, and then to apply them to the analysis of bistatic data collected by the Cassini spacecraft during Titan's flybys.

What is shown here is just a portion of data, related to Titan's polar regions, out of the total data set inspected so far. Other flybys have been studied but are not reported in

horizontally and vertically for clarity purpose. The peaks of the two polarizations are actually at the same frequency value

this document. Here, a good example of both quantitative and qualitative considerations built upon bistatic radar data about the surface of the largest satellite of Saturn is presented. Because of the lack of any publication about the same set of data, we have been careful in highlighting both promising and critical aspects of our results. A large effort was spent to provide reasonable explanations, when possible, to the presented outputs, based on both the comparison with different reports about bistatic radar and personal critical judgement.

Titan's wide polar seas of liquid hydrocarbons showed a perfectly mirror-like behavior, with unprecedented values of rms slope upper limited by 0.01° , and the very strong amplitude of the narrow spikes of their echoes required "ad hoc" corrections to the basic fit template technique proposed by Simpson and Tyler in [14]. For dry lands, generally smooth

Fig. 13 Surface rms slope in degrees against time, latitude and longitude of the antenna boresight intersection with Titan's surface. Values of surface roughness are inferred from the RCP component of the echoes

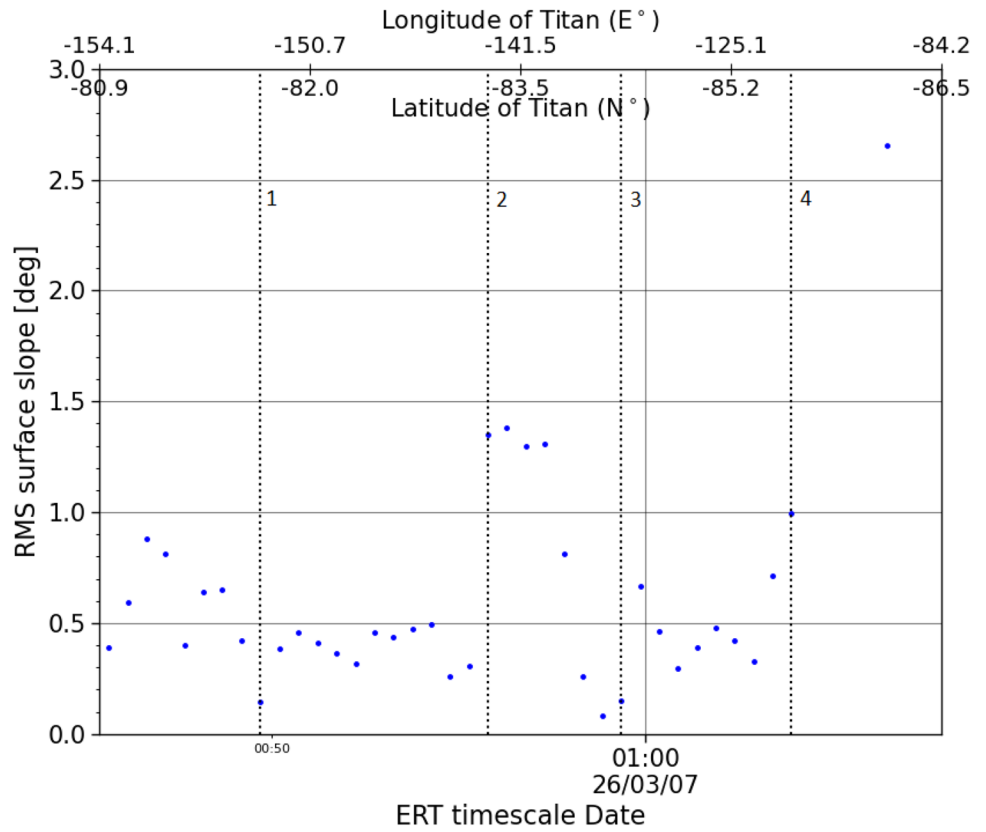
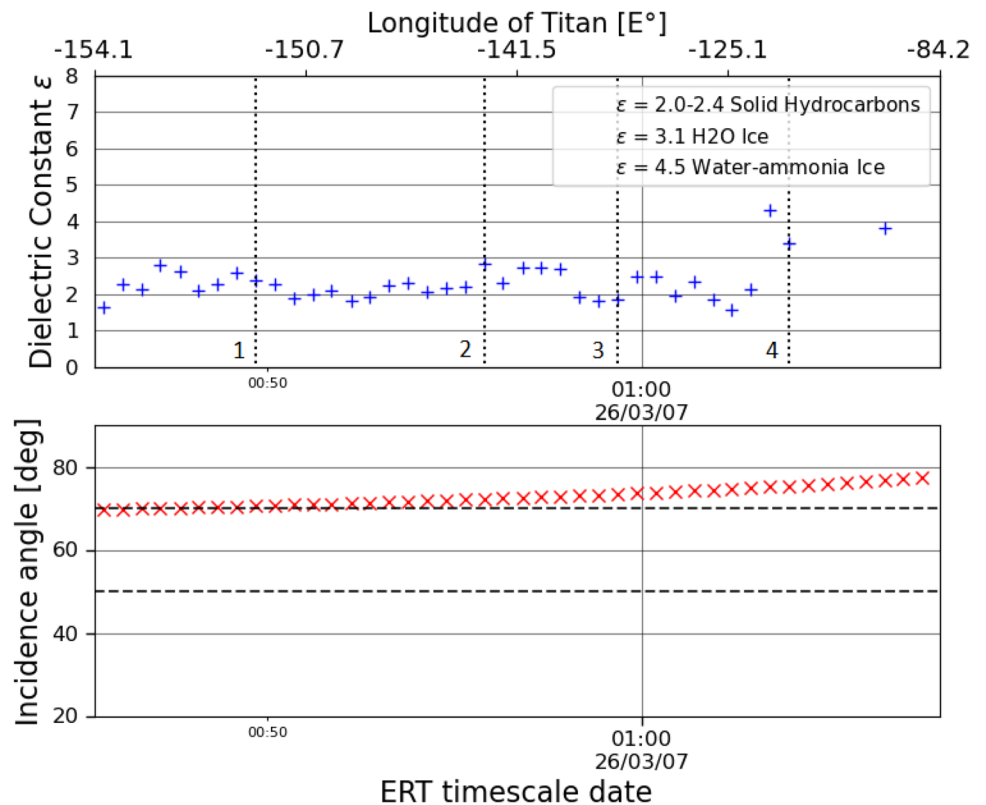


Fig. 14 Dielectric constant estimates and incidence angles of observation against time and longitude of Cassini's HGA boresight intersection with Titan's surface. Ranges of dielectric constant for dry materials expected to be over Titan's surface are listed in the legend. The four positions of interest along the specular point track are highlighted



profiles have been found, and some patches of terrain did not exhibit any quasi-specular reflection towards Earth, because of the inapplicability of the quasi-specular model or the high values of incidence angle. To further validate the computed values of rms surface slope, problems of beam-limitation, diffuse scattering removal, and estimation of the broadening due to the fast shift of the specular point should be dealt with. In the near future, we plan to increase the frequency resolution of reflections from Titan's seas to characterize their roughness more accurately. In addition to this, a future comparison between results in different bands, considering S- and Ka-bands alongside the X-band, may provide insightful information for a better understanding of Titan's surface [17]. Once a larger set of data is confidently analyzed, inferred roughness profiles over longitude and latitude of the planet may be used to locate nominally smooth sites for future landers and rovers.

Dielectric constants were, on average, a bit low for the northern pole, probably because of the lack of a proper absolute calibration. A frequency resolution increase should improve the scattering of the outputs for Titan's liquid surfaces, and this is a check we would like to implement as soon as possible. Observations of the southern pole produced relative dielectric constants consistent with the expected numbers, with a promising smoothness of the output profile highlighting longitudinal and latitudinal differences in solid, liquid hydrocarbons and water ice distribution. In the near future, the absolute calibration of the received signals is of prior importance to improve our results.

What has been carried out was built upon preliminary assumptions, basic techniques and qualitative considerations about the main issues of the field (beam limitation, antenna pointing, validity of the model for grazing angles, and so on). Additional work is required to develop further the preliminary results assessed here, confirming or discarding them. As a matter of fact, now a first-order reference about Cassini bistatic radar data is available.

At the current state of the art, bistatic radar works as a valuable source of complementary data for the validation of, and comparison with, measurements gathered by other instruments, especially considering the potential of inspecting the scattering properties of the surface from a more versatile perspective than monostatic radars and Earth-based observations. Yet, the outputs of this experiment are affected by various uncertainties, that nowadays pose limitations to the role that this instrument could play as a standalone tool for the a-priori inference of planetary surface properties.

Appendix A Specular Point computation

The model of Titan shape we used is a triaxial ellipsoid, with principal axes of $a = 2575.124$ km, $b = 2574.746$ km and $c = 2574.414$ km [36]. The specular point $\mathbf{x} = (x, y, z)$,

expressed in a body-fixed frame rotating with Titan and aligned with the three axes of its ellipsoid (IAU_TITAN), was computed solving a nonlinear system of equations based on geometric considerations. Given that \mathbf{r} and \mathbf{t} are respectively Earth and Cassini positions in IAU_TITAN, $\mathbf{n}(\mathbf{x})$ is the unit vector normal to the ellipsoid of Titan at point \mathbf{x} , and $\hat{LoS} = \frac{\mathbf{r}-\mathbf{t}}{\|\mathbf{r}-\mathbf{t}\|}$ is the line of sight from Cassini to the Earth.

The nonlinear system of equations that we solved to find the specular point is the following:

$$\frac{x^2}{a^2} + \frac{y^2}{b^2} + \frac{z^2}{c^2} = 1 \quad (13)$$

$$[\mathbf{x} - \mathbf{t} \quad \mathbf{n}(\mathbf{x}) \quad \hat{LoS}] = \begin{bmatrix} x - t_x & n_x(\mathbf{x}) & LoS_x \\ y - t_y & n_y(\mathbf{x}) & LoS_y \\ z - t_z & n_z(\mathbf{x}) & LoS_z \end{bmatrix} = 0 \quad (14)$$

$$\frac{\mathbf{r} - \mathbf{x}}{\|\mathbf{r} - \mathbf{x}\|} \cdot \mathbf{n}(\mathbf{x}) - \frac{\mathbf{t} - \mathbf{x}}{\|\mathbf{t} - \mathbf{x}\|} \cdot \mathbf{n}(\mathbf{x}) = 0 \quad (15)$$

Each equation of the system is a geometric constraint about the specular point. Equation (13) requires \mathbf{x} to belong to the ellipsoid of Titan, Eq. (14) requires \mathbf{x} to be part of the plane containing the transmitter \mathbf{t} , the receiver \mathbf{r} , and the local normal $\mathbf{n}(\mathbf{x})$, while Eq. (15) satisfies the specular condition of incidence angle equal to angle of reflection.

The initial guess for the resolution of the system is the intersection between the surface of Titan and the bisector between \mathbf{t} and \mathbf{r} . The specular point is later converted in rectangular coordinates: longitude, latitude and radius in IAU_TITAN.

The quality of the estimate is eventually checked comparing the direction of a specularly reflected ray scattered by the guessed specular point with the line of sight between guessed specular point and receiver. The angular separation between the two vectors is quantified, and plotted against time to spot outliers in the numerical routine. No outlier has been observed, and the rms of the angular separation is in the order of 10^{-4} degrees.

Acknowledgements I would like to thank my supervisors Marco Zannoni, Andrea Togni and Paolo Tortora for the opportunity of working within the Radio Science and Planetary Exploration Laboratory at the University of Bologna, previously as a student and now as a PhD candidate, and for their support, patience, trust and guidance through this research activity. I would also like to thank Dustin Buccino, Daniel Kahan and Kamal Oudrhiri from the Jet Propulsion Laboratory, who are still providing me support for this research, for their availability and fruitful discussions about RSR, data processing and DSN calibration procedures. Lastly, I gratefully acknowledge the incredible value of the past work by Professor Essam Marouf from San Jose State University, for the design of Cassini bistatic observations and for his preliminary inspections of Titan's reflected echoes presented during the Cassini Radio Science Team Meetings. I found these documents, left as part of the Cassini Radio Science Experiments archives, extremely useful to

select the flybys and receiving stations to study first, and I took inspiration from his way of presenting some of the results.

Funding Open access funding provided by Alma Mater Studiorum - Università di Bologna within the CRUI-CARE Agreement.

Declarations

Conflict of interest The author declares that he has no conflict of interest.

Open Access This article is licensed under a Creative Commons Attribution 4.0 International License, which permits use, sharing, adaptation, distribution and reproduction in any medium or format, as long as you give appropriate credit to the original author(s) and the source, provide a link to the Creative Commons licence, and indicate if changes were made. The images or other third party material in this article are included in the article's Creative Commons licence, unless indicated otherwise in a credit line to the material. If material is not included in the article's Creative Commons licence and your intended use is not permitted by statutory regulation or exceeds the permitted use, you will need to obtain permission directly from the copyright holder. To view a copy of this licence, visit <http://creativecommons.org/licenses/by/4.0/>.

References

- Simpson, R.A.: Spacecraft studies of planetary surfaces using bistatic radar. *IEEE Trans. Geosci. Remote. Sens.* **31**(2), 465–482 (1993). <https://doi.org/10.1109/36.214923>
- Simpson, R.A., Tyler, G.L., Pätzold, M., Häusler, B., Asmar, A.W., Sultan-Salem, A.K.: Polarization in bistatic radar probing of planetary surfaces: Application to mars express data. *Proceedings of the IEEE* **99** (2011). <https://doi.org/10.1109/JPROC.2011.2106190>
- Simpson, R.A.: Venus express bistatic radar: high-elevation anomalous reflectivity. *J. Geophys. Res.* (2009). <https://doi.org/10.1029/2008JE003156>
- Palmer, E.M., Heggy, E., Kofman, W.: Orbital bistatic radar observations of asteroid vesta by the dawn mission. *Nat. Commun.* (2017). <https://doi.org/10.1038/s41467-017-00434-6>
- Black, G.J., Campbell, D.B., Carter, L.M.: Ground-based radar observations of titan: 2000–2008. *Icarus* (2011). <https://doi.org/10.1016/j.icarus.2010.10.025>
- Grima, C., Matrogiuseppe, M., Hayes, A.G., Wall, S.D., Lorenz, R.D., Hogfartner, J.D., Stiles, B., Elachi, C., The Cassini RADAR Team: Surface roughness of titan's hydrocarbon seas. *Earth Planet Sci. Lett.* **474**, 20–24 (2017). <https://doi.org/10.1016/j.epsl.2017.06.007>
- Wye, L.C.: Radar scattering from titan and saturn's icy satellites using the cassini spacecraft. Ph.D. thesis (2011)
- Sultan-Salem, A.K., Tyler, G.L.: Modeling quasi-specular scattering from the surface of titan. *J. Geophys. Res.* (2007). <https://doi.org/10.1029/2006JE002878>
- Asmar, S.W., Lazio, J., Atkinson, D.H., Bell, D.J., Broder, J.S., Grudinin, I.S., Mannucci, A.J., Paik, M., Preston, R.A.: Future of planetary atmospheric, surface, and interior science using radio and laser links. *Radio Sci.* **54**(4), 365–377 (2019). <https://doi.org/10.1029/2018RS006663>
- Simpson, R.A.: Planetary exploration. In: Willis, N.J., Griffiths, H.D. (eds.) *Advances in Bistatic Radar*, pp. 56–77. SciTech Publishing Inc. (2007)
- Asmar, S.W., French, R.G., Marouf, E.A., Schinder, P., Armstrong, J.W., Tortora, P., Iess, L., Anabtawi, A., Kliore, A.J., Parisi, A.J., Zannoni, M., Kahan, D.: Cassini radio science user's guide. Cassini Mission Archive Home - PDS Atmospheres Node. https://pds-atmospheres.nmsu.edu/data_and_services/atmospheres_data/Cassini/logs/Cassini%20Radio%20Science%20Users%20Guide%20-%2030%20Sep%202018.pdf (2018). Accessed 7 Sept 2022
- Fjeldbo, G.: Bistatic-radar methods for studying planetary ionospheres and surfaces. Radioscience Laboratory, Stanford University, Tech Rep, Stanford, California (1964)
- Tyler, G.L., Simpson, R.A., Moore, H.J.: Lunar slope distributions: comparison of bistatic-radar and photographic results. *J. Geophys. Res.* (1971). <https://doi.org/10.1029/JB076i011p02790>
- Simpson, R.A., Tyler, G.L.: Viking bistatic radar experiment: summary of first-order results emphasizing north polar data. *Icarus* (1981). [https://doi.org/10.1016/0019-1035\(81\)90139-1](https://doi.org/10.1016/0019-1035(81)90139-1)
- Palmer, E.M., Heggy, E.: Bistatic radar occultations of planetary surfaces. *IEEE Geosci. Remote. Sens. Lett.* **17**(5), 804–808 (2020). <https://doi.org/10.1109/LGRS.2019.2931310>
- Campbell, B.A., Shepard, M.K.: Lava flow surface roughness and depolarized radar scattering. *J. Geophys. Res.* (1996). <https://doi.org/10.1029/95JE01804>
- Tyler, G.L., Howard, H.T.: Dual-frequency bistatic-radar investigations of the moon with Apollos 14 and 15. *J. Geophys. Res.* (1973). <https://doi.org/10.1029/JB078I023P04852>
- Wye, L.C., Zebker, H.A., Ostro, S.J., West, R.D., Gim, Y., Lorenz, R.D., The Cassini RADAR Team: Electrical properties of titan's surface from Cassini radar scatterometer measurements. *Icarus* **188**(2), 367–385 (2007). <https://doi.org/10.1016/j.icarus.2006.12.008>
- Lorenz, R.D., Biolluz, G., Encrenaz, P., Janssen, M.A., West, R.D., Muhleman, D.O.: Cassini radar: prospects for titan surface investigations using the microwave radiometer. *Planet. Space Sci.* **51**, 353–364 (2003). [https://doi.org/10.1016/S0032-0633\(02\)00148-4](https://doi.org/10.1016/S0032-0633(02)00148-4)
- Phillippe, P., Lunine, J., Ruffié, G., Pierre, E., Wall, S., Lorenz, R., Janssen, R.: Microwave dielectric constant of titan-relevant materials. *Geophys. Res. Lett.* (2008). <https://doi.org/10.1029/2008GL035216>
- Taylor, J., Sakamoto, L., Wong, C.: Article 3 Cassini orbiter/huygens probe telecommunications. DESCANSO - Deep Space Communications and Navigation Center of Excellence. <https://descanso.jpl.nasa.gov/DPSummary/Descanso3--Cassini2.pdf> (2002). Accessed 7 Sept 2022
- Simpson, R.A., Tyler, G.L., Campbell, D.B.: Arecibo radar observations of Martian surface characteristics near the equator. *Icarus* **33**, 102–115 (1978). [https://doi.org/10.1016/0019-1035\(78\)90027-1](https://doi.org/10.1016/0019-1035(78)90027-1)
- Simpson, R.A., Tyler, G.L., Campbell, D.B.: Arecibo radar observations of mars surface characteristics in the northern hemisphere. *Icarus* **36**, 153–173 (1978). [https://doi.org/10.1016/0019-1035\(78\)90101-X](https://doi.org/10.1016/0019-1035(78)90101-X)
- Tyler, G.L., Simpson, R.A.: Bistatic radar measurements of topographic variations in lunar surface slopes with explorer 35. *Radio Sci.* **5**, 263–271 (1970). <https://doi.org/10.1029/RS005i002p00263>
- Deep Space Mission System (DSMS) External Interface Specification 0159-Science Radio Science Receiver Standard Formatted Data Unit (SDFU), part of the DSN document 820-013 (JPL D-16765). Jet Propulsion Laboratory, Pasadena, CA. https://pds-geosciences.wustl.edu/radioscience/docs/urn-nasa-pds-radiosci_documentation/dsn_0159-science/dsn_0159-science.2009-05-18.txt (2009). Accessed 7 Sept 2022

26. Simpson, R.A., Tyler, G.L., Pätzold, G.L., Häusler, B.: Determination of local surface properties using mars express bistatic radar. *J. Geophys. Res.* (2006). <https://doi.org/10.1029/2005JE002580>
27. Stelzried, C.T., Klein, M.J.: Precision DSN radiometer systems: impact on microwave calibrations. *Proc. IEEE* **82**(5), 776–787 (1994). <https://doi.org/10.1109/5.284745>
28. Poggiali, V., Hayes, A.G., Mastrogiuseppe, M., Le Gall, A., Lalich, D., Gómez-Leal, I., Lunine, J.I.: The bathymetry of moray sinus at titan's kraken mare. *J. Geophys. Res. Planet.* (2020). <https://doi.org/10.1029/2020JE006558>
29. Zebker, H., Hayes, H., Janssen, M., Le Gall, A., Lorenz, R., Wye, L.: Surface of Ligeia mare, titan, from Cassini altimeter and radiometer analysis. *Geophys. Res. Lett.* (2014). <https://doi.org/10.1002/2013GL058877>
30. Stephan, K., Jaumann, R., Brown, R.H., Soderblom, J., Soderblom, L., Barnes, J., Sotin, C., Griffith, C., Kirk, R., Baines, K., Buratti, B., Clark, R., Lytle, D., Nelson, R., Nicholson, P.: Specular reflection on titan: liquids in kraken mare. *Geophys. Res. Lett.* **37**(7), 1–5 (2010). <https://doi.org/10.1029/2009GL042312>
31. Dahl, P.: On bistatic seas surface scattering: field measurements and modeling. *J. Acoust. Soc. Am.* (1999). <https://doi.org/10.1121/1.426820>
32. Gleason, S., Zavorotny, V.U., Akos, D.M., Hrbek, S., PopStefanija, I., Walsh, E.J., Masters, D., Grant, M.S.: Study of surface wind and mean square slope correlation in hurricane ike with multiple sensors. *IEEE J. Sel. Topics Appl. Earth Observ. Remote Sens.* **11**(6), 1975–1988 (2018). <https://doi.org/10.1109/JSTARS.2018.2827045>
33. Hayes, A.G., Lorenz, R.D., Donelan, M.A., Manga, M., Lunine, J., Schneider, T., Lamb, M.P., Mitchell, J.M., Fischer, W.W., Graves, S.D., Tolman, H.L., Aharonson, O., Encrenaz, P.J., Ventura, B., Casarano, D., Notarnicola, C.: Wind driven capillary-gravity waves on Titan's lakes: hard to detect or non-existent? *Icarus* **225**(1), 403–412 (2013). <https://doi.org/10.1016/j.icarus.2013.04.004>
34. ...Lopes, R.M.C., Wall, S.D., Elachi, C., Birch, S.P.D., Corlies, P., Coustenis, A., Hayes, A.G., Hofgartner, J.D., Janssen, M.A., Kirk, R.L., LeGall, A., Lorenz, R.D., Lunine, J.I., Malaska, M.J., Mastrogiuseppe, M., Mitri, G., Neish, C.D., Noranicola, C., Paganelli, F., Paillou, P., Poggiali, V., Radebaugh, J., Rodriguez, S., Schoenfeld, A., Soderblom, J.M., Solomonidou, A., Stofan, E.R., Stiles, B.W., Tosi, F., Turtle, E.P., West, R.D., Wood, C.A., Zebker, H.A., Barnes, J.W., Casarano, D., Encrenaz, P., Farr, T., Grima, C., Hemingway, D., Karatekin, O., Lucas, A., Mitchell, K.L., Ori, G., Orosei, R., Ries, P., Riccio, D., Soderblom, L.A., Zang, Z.: Titan as revealed by the Cassini radar. *Space Sci. Rev.* (2019). <https://doi.org/10.1007/s11214-019-0598-6>
35. Vesecky, J.F., Sperley, E.J., Zebker, H.: Electromagnetic wave scattering at near-grazing incidence from a gently undulating, rough surface (1988). Paper presented at the 88th International Geoscience and Remote Sensing Symposium: 'Remote Sensing Moving Toward the 21st Century', Edinburgh, UK, 12–16 Sept 1988 <https://doi.org/10.1109/IGARSS.1988.569527>
36. Corlies, P., Hayes, A.G., Birch, S.P.D., Lorenz, R., Stiles, B.W., Kirk, R., Poggiali, V., Zebker, H., Iess, L.: Titan's topography and shape at the end of the Cassini mission. *Geophys. Res. Lett.* **44**(23), 754–761 (2017). <https://doi.org/10.1002/2017GL075518>

Publisher's Note Springer Nature remains neutral with regard to jurisdictional claims in published maps and institutional affiliations.